



JADES Initial Data Release for the Hubble Ultra Deep Field: Revealing the Faint Infrared Sky with Deep JWST NIRC*am* Imaging

Marcia J. Rieke¹, Brant Robertson², Sandro Tacchella^{3,4}, Kevin Hainline¹, Benjamin D. Johnson⁵, Ryan Hausen⁶, Zhiyuan Ji¹, Christopher N. A. Willmer¹, Daniel J. Eisenstein⁵, Dávid Puskás^{3,4}, Stacey Alberts¹, Santiago Arribas⁷, William M. Baker^{3,4}, Stefi Baum⁸, Rachana Bhatawdekar⁹, Nina Bonaventura¹, Kristan Boyett^{10,11}, Andrew J. Bunker¹², Alex J. Cameron¹², Stefano Carniani¹³, Stephane Charlot¹⁴, Jacopo Chevallard¹², Zuyi Chen¹, Mirko Curti^{3,4}, Emma Curtis-Lake¹⁵, A. Lola Danhaive⁴, Christa DeCoursey¹, Alan Dressler¹⁶, Eiichi Egami¹, Ryan Endsley¹⁷, Jakob M. Helton¹, Raphael E. Hviding^{1,18}, Nimisha Kumari¹⁹, Tobias J. Looser^{3,4}, Jianwei Lyu¹, Roberto Maiolino^{3,4,20}, Michael V. Maseda²¹, Erica J. Nelson²², George Rieke¹, Hans-Walter Rix¹⁸, Lester Sandles^{3,4}, Aayush Saxena²⁰, Katherine Sharpe⁵, Irene Shvaei^{1,7}, Maya Skarbinski⁵, Renske Smit²³, Daniel P. Stark¹, Meredith Stone¹, Katherine A. Suess^{24,25}, Fengwu Sun¹, Michael Topping¹, Hannah Übler^{3,4}, Natalia C. Villanueva⁵, Imaan E. B. Wallace¹², Christina C. Williams²⁶, Chris Willott²⁷, Lily Whitler¹, Joris Witstok^{3,4}, and Charity Woodrum¹

¹ Steward Observatory, University of Arizona, 933 N. Cherry Avenue, Tucson, AZ 85721, USA; mrieke@arizona.edu

² Department of Astronomy and Astrophysics, University of California, Santa Cruz, 1156 High Street, Santa Cruz, CA 95064, USA

³ Cavendish Laboratory, University of Cambridge, 19 JJ Thomson Avenue, Cambridge CB3 0HE, UK

⁴ Kavli Institute for Cosmology, Madingley Road, Cambridge CB3 0HA, UK

⁵ Center for Astrophysics | Harvard and Smithsonian, 60 Garden Street, Cambridge, MA 02138, USA

⁶ Department of Physics and Astronomy, Johns Hopkins University, 3400 N. Charles Street, Baltimore, MD 21218, USA

⁷ Centro de Astrobiología (CAB), CSIC-INTA, Cra. de Ajalvir Km. 4, E-28850 Torrejón de Ardoz, Madrid, Spain

⁸ Department of Physics and Astronomy, University of Manitoba, Winnipeg, MB R3T 2N2, Canada

⁹ European Space Agency, ESA/ESTEC, Keplerlaan 1, 2201 AZ Noordwijk, The Netherlands

¹⁰ School of Physics, University of Melbourne, Parkville 3010, VIC, Australia

¹¹ ARC Centre of Excellence for All Sky Astrophysics in 3 Dimensions (ASTRO 3D), Australia

¹² Department of Physics, University of Oxford, Denys Wilkinson Building, Keble Road, Oxford OX1 3RH, UK

¹³ Scuola Normale Superiore, Piazza dei Cavalieri 7, I-56126 Pisa, Italy

¹⁴ Sorbonne Université, UPMC-CNRS, UMR7095, Institut d'Astrophysique de Paris, F-75014 Paris, France

¹⁵ Centre for Astrophysics Research, Department of Physics, Astronomy and Mathematics, University of Hertfordshire, Hatfield AL10 9AB, UK

¹⁶ The Observatories of the Carnegie Institution for Science, 813 Santa Barbara Street, Pasadena, CA 91101, USA

¹⁷ Department of Astronomy, University of Texas, Austin, TX 78712 USA

¹⁸ Max-Planck-Institut für Astronomie, Königstuhl 17, D-69117, Heidelberg, Germany

¹⁹ AURA for European Space Agency, Space Telescope Science Institute, 3700 San Martin Drive, Baltimore, MD 21218, USA

²⁰ Department of Physics and Astronomy, University College London, Gower Street, London WC1E 6BT, UK

²¹ Department of Astronomy, University of Wisconsin–Madison, 475 N. Charter Street, Madison, WI 53706, USA

²² Department for Astrophysical and Planetary Science, University of Colorado, Boulder, CO 80309, USA

²³ Astrophysics Research Institute, Liverpool John Moores University, 146 Brownlow Hill, Liverpool L3 5RF, UK

²⁴ Department of Astronomy and Astrophysics, University of California, Santa Cruz, Santa Cruz, CA 95064, USA

²⁵ Kavli Institute for Particle Astrophysics and Cosmology and Department of Physics, Stanford University, Stanford, CA 94305, USA

²⁶ NSF's National Optical-Infrared Astronomy Research Laboratory, 950 North Cherry Avenue, Tucson, AZ 85719, USA

²⁷ NRC Herzberg, 5071 West Saanich Road, Victoria, BC V9E 2E7, Canada

Received 2023 June 3; revised 2023 August 22; accepted 2023 August 24; published 2023 October 27

Abstract

JWST has revolutionized the field of extragalactic astronomy with its sensitive and high-resolution infrared view of the distant Universe. Adding to the new legacy of JWST observations, we present the first NIRC*am* imaging data release from the JWST Advanced Deep Extragalactic Survey (JADES), providing nine filters of infrared imaging of ~ 25 arcmin² covering the Hubble Ultra Deep Field and portions of Great Observatories Origins Deep Survey South. Utilizing 87 on-sky dual-filter hours of exposure time, these images reveal the deepest ever near-infrared view of this iconic field. We supply carefully constructed nine-band mosaics of the JADES bands, as well as matching reductions of five additional bands from the JWST Extragalactic Medium-band Survey. Combining with existing Hubble Space Telescope imaging, we provide 23-band space-based photometric catalogs and photometric redshifts for $\approx 47,500$ sources. To promote broad engagement with JADES, we have created an interactive *FitsMap* website to provide an interface for professional researchers and the public to experience these JWST data sets. Combined with the first JADES NIRS*pec* data release, these public JADES imaging and spectroscopic data sets provide a new foundation for discoveries of the infrared Universe by the worldwide scientific community.

Unified Astronomy Thesaurus concepts: [High-redshift galaxies \(734\)](#)

1. Introduction

An essential route to the study of the early history of galaxies is the detection and characterization of incredibly distant galaxies, utilizing the finite light-travel time to see galaxies in



Original content from this work may be used under the terms of the [Creative Commons Attribution 4.0 licence](#). Any further distribution of this work must maintain attribution to the author(s) and the title of the work, journal citation and DOI.

their youth. This has driven astronomers to build and use telescopes to study extremely faint and small galaxies. The James Webb Space Telescope (JWST; Gardner et al. 2023) is the next great step, optimized for the essential wavelengths in the infrared and equipped with extremely flexible and capable instruments. The first year of the mission has revealed high-redshift galaxies as never before possible (Robertson et al. 2023; Curtis-Lake et al. 2023).

In the past three decades, astronomers have focused increasingly on deep blank-field surveys, as these give an unbiased selection of high-redshift galaxies, the populations of which reveal themselves at the faintest technological limits. A famous step in this quest was the Hubble Deep Field (HDF; Williams et al. 1996; Ferguson et al. 2000), which revealed a dazzling array of galaxies beyond redshift $z \sim 3$. This prompted heavy investment from many large telescopes in this field, as well as in a southern companion, the Chandra Deep Field South (Giacconi et al. 2002), and both fields were expanded in the Great Observatories Origins Deep Survey (GOODS; Giavalisco et al. 2004). Soon after, the Hubble Ultra Deep Field (HUDF), the deepest optical image yet taken, was observed at the center of the GOODS-S field (Beckwith et al. 2006).

NICMOS was used for the first space-based infrared observations of the HDF (Thompson et al. 1999). Other studies such as Conselice et al. (2011) exploited the capabilities provided by NICMOS to study the evolution of massive galaxies. The installation of Wide Field Camera 3 on the Hubble Space Telescope (HST) afforded improved infrared sensitivity and a substantially wider field of view, which led to much deeper 1–2 μm imaging (e.g., Bouwens et al. 2010; Oesch et al. 2010). This improved infrared imaging provided much larger $z \sim 7$ samples than previously available.

The two deep fields GOODS-S and GOODS-N, as well as a small number of others, have attracted enormous collective attention from essentially every large narrow-field telescope in the world, as astronomers interested in the faint extragalactic sky pour their new investments of observing time into the fields to take advantage of the previous investments. The HUDF has remained the premier field, with contributions too numerous to list but hosting the deepest general-purpose extragalactic images at nearly all common wavelengths. Key examples include very deep HST infrared images, such as from the HUDF09 and HUDF12 program (Ellis et al. 2013; Illingworth et al. 2013), the continued investment of Chandra imaging (e.g., Xue et al. 2016), deep Atacama Large Millimeter/submillimeter Array observations (Aravena et al. 2016; Walter et al. 2016; Dunlop et al. 2017; Hatsukade et al. 2018), deep Very Large Array imaging (e.g., Rujopakarn et al. 2016), and large investments of spectroscopy, such as with the Multi Unit Spectroscopic Explorer (MUSE) on the Very Large Telescope (e.g., Bacon et al. 2017, 2021).

With the JWST Advanced Deep Extragalactic Survey (JADES), we aim to continue the legacy of the GOODS-S/HUDF and GOODS-N/HDF fields, bringing extremely deep high-quality JWST near-infrared imaging and spectroscopy to the field. JADES is a collaboration of the JWST Near-Infrared Camera (NIRCam) and Near-Infrared Spectrograph instrument development teams, pooling about 770 hr of guaranteed time of the mission to the purpose of executing a carefully crafted survey of the fields (Eisenstein et al. 2023).

Here we present the initial data release of NIRCam imaging from JADES, covering 25 arcmin² on and around the HUDF.

This nine-band imaging includes 87 open-shutter hours of dual-filter imaging, comprising about 111 hr of mission time. Exposure times range from ~ 14 to ~ 60 ks per filter. Our release mosaics and catalogs include five further bands from the JWST Extragalactic Medium-band Survey (JEMS; Williams et al. 2023), which covers one-third of the release area. A companion paper (Bunker et al. 2023) presents deep spectroscopy on the HUDF.

We describe the data included in this release in Section 2, the image-processing methodology in Section 3, and the photometry methods in Section 4. In Section 5, we summarize the quantitative performance assessment and validation of the images and catalogs, although further information will be presented in S. Tacchella et al. (2023, in preparation) and B. Robertson et al. (2023, in preparation). Section 6 presents a set of photometric redshifts computed from the catalog, utilizing up to 14 JWST bands and 5 HST ACS bands, with full details provided by Hainline et al. (2023). We conclude in Section 7.

2. Data Release Contents

The imaging portion of this first JADES data release comes from the NIRCam imaging of program 1180 (PI: Eisenstein), observations 7, 10, 11, 15, 17, and 18. These are half of the Deep Prime mosaic, covering the HUDF, and a log of the observations is presented in Table 1, which tabulates several parameters used in the Astronomer’s Proposal Tool, used to identify the observation, namely, the pointing name, the observation number, the name associated with pointing (TARGPROP), the visit identification, and the starting and ending UT dates of the observation. As described in Eisenstein et al. (2023), observations 7, 10, 15, and 18 form a 2×2 overlapping mosaic of pointings, each a nine-point dither of five filter pairs. Observations 11 and 17 add another eight-point dither, building depth in three of the filter pairs in two of the pointings. Each exposure is 1375 s. These data were acquired from 2022 September 29 through October 5, at which time the zodiacal light background was low. Figure 1 shows the layout of this data release along with the outlines of other datasets acquired in this area.

Nine total filters are provided in these JADES data: F090W, F115W, F150W, F200W, F277W, F335M, F356W, F410M, and F444W. The two medium-band filters, F335M and F410M, provide extra spectral resolution in the 3–5 μm region that samples the rest-frame optical band at high redshift. In so doing, we reveal strong emission lines and provide measurement of the stellar continuum between them.

The total area covered by these observations is about 25 arcmin², but the area covered in the shortwave (SW) and longwave (LW) arms of NIRCam is not identical. A sizable portion of the area is covered by two pointings, substantially increasing the depth. There are two thin uncovered strips in F200W owing to the SW chip gap; these were covered in other filters and will be covered in F200W in year 2 JADES observing. We mention that the area covered in all nine filters is set by the intersection of the F200W and F356W footprints.

We combine the JADES data with imaging from JEMS (program 1963; Williams et al. 2023). JEMS imaged one NIRCam field in five medium-band filters, F182M, F210M, F430M, F460M, and F480M. While not as deep as the JADES data, these filters provide additional resolution on the spectral energy distributions, and these images reveal more emission

Table 1
Log of NIRCcam Observations

Pointing	Observation	TARGPROP	VISIT_ID	Start Date	End Date
Deep Pointing 1 Part 1	7	POINTINGONE-B	01180007001	2022-09-29	2022-09-30
Deep Pointing 2 Part 1	10	POINTINGTWO-B	01180010001	2022-09-30	2022-10-01
Deep Pointing 2 Part 2	11	POINTINGTWO-C	01180011001	2022-10-03	2022-10-04
Deep Pointing 3 Part 3	15	POINTINGTHREE-A	01180015001	2022-10-04	2022-10-05
Deep Pointing 4 Part 2	17	POINTINGFOUR-C	01180017001	2022-10-05	2022-10-05
Deep Pointing 4 Part 3	18	POINTINGFOUR-A	01180018001	2022-10-02	2022-10-03

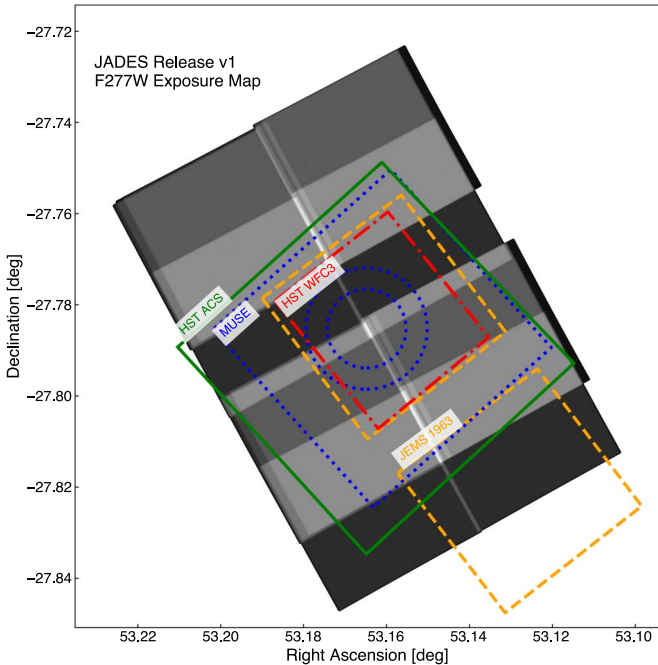


Figure 1. Field layout of the first JADES data release images relative to other surveys in the GOODS-S region. The coverage of the JADES F277W imaging in this first data release is shown as a grayscale image and is representative of the coverage in each JADES filter. This portion of JADES covers the HST WFC3 Ultra Deep Field (red dashed-dotted; Ellis et al. 2013; Illingworth et al. 2013), the HST ACS Ultra Deep Field (green solid; Beckwith et al. 2006), the MUSE Ultra Deep Field mosaic (blue dotted square; Bacon et al. 2017), and the MUSE Extremely Deep Field (blue dotted circle; Bacon et al. 2021). The blue circles outline the 10 and 100 hr MUSE exposure depths. JEMS (Williams et al. 2023), shown with an orange dashed line, overlaps with the HST UDF and the JADES NIRCcam imaging. We incorporate the JEMS imaging into this release, with uniform processing.

lines over a larger range of redshifts in these high-redshift galaxies.

Table 2 summarizes the exposures and achieved sensitivities. In all 14 filters, JADES and JEMS provide extensive pixel diversity, allowing substantial mitigation of flat-fielding errors, cosmic rays, and other pixel-level issues. This proved important in the JADES data, as four of the observations suffer from substantial persistence in three of the eight SW detectors. These are described more in Eisenstein et al. (2023). Our masking mitigations are described in Section 3.3.2.

3. Data Processing and Mosaics

We give here an overview of how we reduce JADES and JEMS NIRCcam data and construct the final mosaics that are part of this release. A more detailed discussion of the procedure including quality assessments will be presented in S. Tacchella et al. (2023, in preparation). We process the images with the

JWST Calibration Pipeline (v1.9.6) with custom steps and modifications as described below. For this first public release, we use Calibration Reference Data System pipeline mapping (CRDS pmap) 1084, which includes in-flight NIRCcam dark, distortion, bad pixel mask, read noise, superbias, and flat reference files.

3.1. Stage 1 Detector Processing

Stage 1 consists of detector-level corrections that are performed on a group-by-group basis, followed by ramp fitting. In this step, the data quality (DQ) arrays are initialized, saturated pixels are identified, the superbias is subtracted, the readout noise is corrected using the reference pixels, non-linearity corrections are applied, dark current is subtracted, and cosmic rays are identified. NIRCcam suffers from large cosmic-ray events, called “snowballs,”²⁸ which have the characteristics of a cosmic ray surrounded by a halo of pixels that have a low level of excess counts. This halo can be as large as several hundreds of pixels. The JWST Calibration Pipeline constrains and corrects for this halo in the jump step by fitting circles that enclose the large events, expands these circles by the input `expansion_factor`, and marks them as jumps in the DQ array. We find that the identification and correction of snowballs work well in $\sim 80\%$ of the cases, with problems mostly arising from the largest hits. We run Stage 1 with the default parameters. The output of Stage 1 processing is a count-rate image in units of counts per second.

3.2. Stage 2 Imaging Calibration

Stage 2 processing consists of additional instrument-level and observing-mode corrections and calibrations to produce fully calibrated exposures. Specifically, this step involves flat-fielding the data and applying flux calibration that converts the images from counts s^{-1} to $MJy sr^{-1}$. We adopt the default values for these pipeline steps but replace the STScI flats with supersky flats for the JADES and JEMS LW bands. We also apply an astrometric correction, which is needed for the conversion from counts s^{-1} to $MJy sr^{-1}$.

The motivation for constructing our own flats arose by finding distinct small-scale periodic patterns in the background structure of LW module mosaics of the deep JADES observations that resulted in the detection of numerous spurious sources. To mitigate this issue, we created supersky flats for the JADES and JEMS LW bands based on the JADES imaging. This procedure is detailed in S. Tacchella et al. (2023, in preparation)—here we note that our tests indicate that these flat fields perform at least as well as the sky flats released to the Calibration Reference Data System (CRDS) on 2023 May 4.

²⁸ <https://jwst-docs.stsci.edu/jwst-near-infrared-camera/nircam-instrument-features-and-caveats/nircam-claws-and-wisps>

Table 2
Image Mosaic Properties

Filter	Program ID	5σ Flux Depth (nJy)	AB mag 0."3 Diameter	Aperture Correction	Exposure Time 90% (20%) (s)	Area (arcmin ²)
JADES						
F090W	1180	5.8	29.49	1.26	12,368 (35,730)	24.9 (6.3)
F115W	1180	4.3	29.82	1.24	24,737 (60,468)	25.0 (6.7)
F150W	1180	4.6	29.74	1.22	12,368 (35,730)	25.2 (7.3)
F200W	1180	4.4	29.79	1.23	12,368 (24,736)	24.4 (8.0)
F277W	1180	3.4	30.07	1.36	12,368 (35,730)	25.8 (9.4)
F335M	1180	5.9	29.47	1.43	12,368 (24,376)	25.5 (9.8)
F356W	1180	3.6	30.01	1.45	12,368 (24,736)	25.6 (9.9)
F410M	1180	5.7	29.51	1.49	12,368 (35,730)	25.8 (9.4)
F444W	1180	4.5	29.77	1.52	12,368 (35,730)	25.8 (9.4)
JEMS						
F182M	1963	6.1	29.44	1.23	13,914 (27,829)	10.0 (7.0)
F210M	1963	7.2	29.26	1.24	13,914 (27,829)	10.0 (7.0)
F430M	1963	14.5	28.50	1.51	6957 (13,914)	9.8 (8.1)
F460M	1963	18.8	28.21	1.54	6957 (13,914)	9.8 (8.1)
F480M	1963	13.6	28.57	1.57	13,914 (27,829)	9.8 (8.1)

Recent CRDS releases provide flat fields produced in a manner similar to what was used for the JADES mosaics, both of which are an improvement over early flats that were based on ground test data and limited flight data.

Briefly, for each band the flats were generated by first constructing a mosaic and identifying sources in the image through a segmentation map. This mosaic segmentation map was dilated and reprojected to the individual Stage 1 count-rate images. Each masked rate image was divided by its median to produce an estimate of the response of the detectors to a uniform source of illumination. We then computed the median over all rate files. For some medium bands we did not have sufficient images to produce a robust flat field; in these cases we interpolated the flat-field images from the surrounding bands. We found that the use of these flats substantially improved the smoothness of the background in mosaicked images on small scales.

3.3. Custom Steps after Stage 2

Following Stage 2, we perform several custom corrections in order to account for several features in the NIRCcam images (Rigby et al. 2023), including the $1/f$ noise (Schlawin et al. 2020), scattered-light effects²⁹ (“wisps” and “claws”), and the large-scale background. Since all of those effects are additive, we fit and subtract them. Finally, we also updated the DQ array in order to mask additional features that led to an imprint onto the mosaics, including persistence, uncorrected wisp features, and unflagged hot pixels.

3.3.1. $1/f$ Noise and Wisp Subtraction

We assume a parametric model for the $1/f$ noise. We fit the source-masked, background-subtracted image (see below) with a model for the $1/f$ noise

$$D_{x,y} = (a_x + b_{y,\text{amp}} + c_{\text{amp}}), \quad (1)$$

where a is a vector of coefficients of length 2048, b_{amp} are four vectors of coefficients each of length 2048 (one for each

amplifier), and c_{amp} are constants for each of the four amplifiers. This model is fit using a GPU-accelerated code.

We construct the wisp templates from the calibrated Stage 2 images. We include all SW images from PID 1180, 1181, 1210, 1286, 1837, and 1963. Specifically, similar to the flat construction, we dilate and then project the mosaic segmentation map to the individual Stage 2 images. Following this, we subtract a median background from each individual Stage 2 image and then compute a median image for each detector. We also construct a wisp mask that contains the main wisp feature. The detectors with the strongest wisp features are A3, A4, B3, and B4, while A1 shows an “eye”-like feature on the top right.

We then subtract a large-scale background, the scaled wisp template, and the $1/f$ noise from the Stage 2 images. We estimate the large-scale background with the `Photutils Background2D` class, using the `biweight_location` estimator to obtain the average background in sigma-clipped boxes of 256×256 pixels in a grid across the image. The resulting low-resolution background grid is then median-filtered over 3×3 adjacent boxes. After subtracting this large-scale background, we fit the wisp template in the overlapping region of the wisp mask and where no sources are present. After subtracting this normalized wisp template, we fit for and subtract the $1/f$ noise model as outlined above.

3.3.2. Masking

We found several artifacts in the initial mosaics, which are caused by persistence, some residual wisp and claw features, and hot pixels. We visually inspected all the Stage 2 images, looking for remaining artifacts, and manually masked these features to clean the final images. Masks were constructed using the free and open-source raster graphics editor Gimp.³⁰

The persistence is thought to be originating from an observation of the Trapezium region (Program ID 1256) taken only 30 minutes prior to the first JADES observation, which left a substantial imprint on the detectors owing to its high surface brightness. Large-scale persistence is visible in the A3 and B4 detectors, as well as some in the B3 detector, most pronounced in the F090W and F115W filters. Additionally,

²⁹ <https://jwst-docs.stsci.edu/jwst-near-infrared-camera/nircam-instrument-features-and-caveats/nircam-claws-and-wisps>

³⁰ Gimp version 2.10.34 available at <https://www.gimp.org>.

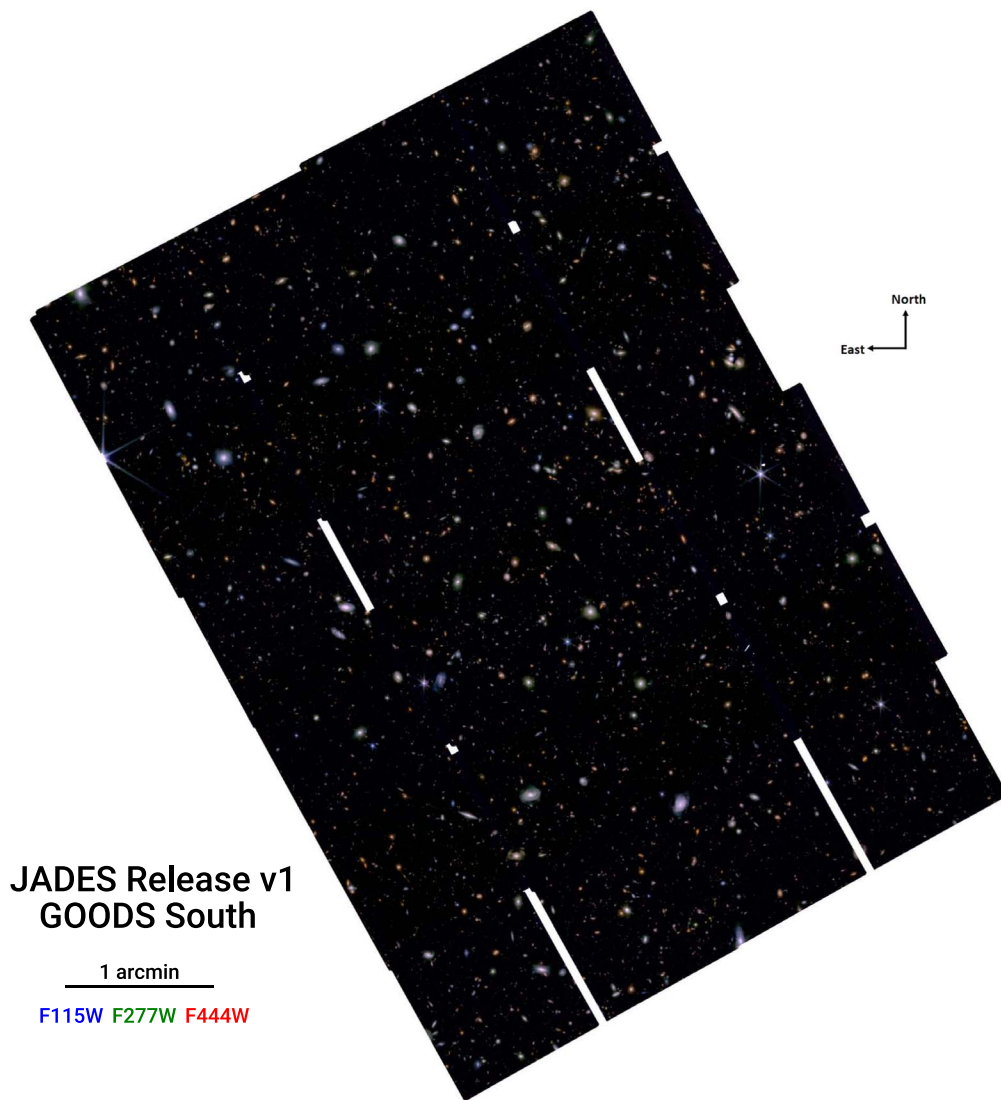


Figure 2. False-color image of the JADES NIRCcam mosaic. Shown are logarithmic scalings of F444W (red), F277W (green), and F115W (blue) filter images on a $0''.3$ -pixel scale. The scale bar indicates $1'$. The white regions are areas with incomplete short-wavelength coverage.

there was strong persistence caused by bright stars and resulting lines from the telescope slewing through possibly a star field in the preceding observations. These features were mainly present in observations 7, 10, 15, and 18. There were some wispy- and claw-related residuals in the filters F150W and F200W, detectors A3, B1, B2, and B4, in particular in observations 11 and 17. Furthermore, a circular feature, dubbed the “eye,” was generally present on detector A1, in F090W and F115W. There were a few cases of uncorrected snowballs that we masked.

All the above features (persistence, wisps, claws, and eye) were easily identifiable since they are stationary on the detector. However, there were two cases of artifacts that were moving with the background and hence could only be identified from the final mosaics. These were hexagon-shaped artifacts near bright stars, which look very similar to the telescope aperture shape. Therefore, we suggest that these are rare cases of filter “ghosts,” which were also previously identified on HST images.³¹

Finally, in the initial mosaic, we found ~ 80 hot pixels across all bands. Most SW hot pixels were related to large cosmic-ray hits, which have not been properly masked in Stage 1. This led to bright pixels, with $DQ = 0$. Those were not picked up by the outlier rejection in Stage 3, because the errors of those pixels were extremely large. We have addressed this by (i) ensuring that neighboring pixels of cosmic-ray hits with fluxes in the top 99.9th percentile are masked and (ii) setting a maximum error of 0.03 in the error maps, which translates into clipping the top 99.99th percentile. Most LW hot pixels appeared on the edges of the mosaics, consistent with having only a few images (≈ 3) in the outlier rejection of Stage 3. We identified those hot pixels in the individual Stage 2 products and added them to those masks.

3.4. Stage 3—Mosaic Construction

Stage 3 combines all the individual images and dithers into a single mosaic per filter. This step includes astrometric alignment, background matching, outlier detection, and resampling the images onto a common output grid. Figure 2 presents a red–green–blue image constructed from three of the

³¹ <https://www.stsci.edu/hst/instrumentation/wfc3/performance/anomalies>

filter mosaics. After a customized astrometric correction, we run Stage 3 with the default parameter values, setting the pixel scale to $0''.03 \text{ pixel}^{-1}$,³² and with a drizzle parameter of $\text{pixfrac} = 1$ for the SW and LW images. We constructed a mosaic for each observation, i.e., a total of six submosaics (observations 7, 10, 11, 15, 17, and 18). We perform a custom background subtraction of those submosaics to remove any residual background before combining them into a final mosaic, ensuring proper flux and error propagation and perfect pixel grid alignment. In the following, we describe briefly these customized processing steps.

Our astrometric alignment process includes some modifications of the standard `jd-st-pipeline tweakreg` procedure. The astrometric alignment of the JADES and JEMS imaging is computed relative to HST images that have been registered to Gaia DR2 (G. Brammer, private communication; Gaia Collaboration et al. 2018). We first construct a reference catalog of isolated, approximately round objects from these Gaia-registered HST F160W and, where F160W imaging is not available, F850LP images. For every Stage 2 NIRC*am* F150W and F200W image in a given observation—consisting of several dither positions taken after the same guide star acquisition—we determine source positions using the `SExtractor` for Python (Barbary 2016) implementation of the `SExtractor` detection code. We then cross-match these sources with the reference catalog and compute the rotation and offset of each level-2 image relative to the reference catalog. Finally, we apply the median rotation and offset for this observation and guide-star acquisition sequence to all level-2 images in a given observation. For images taken in the A module with the medium-band F335M and the JEMS F182M and F210M filters, we replace the default distortion maps with the nearest (in effective wavelength) wide band distortion map for that detector. After this astrometric alignment and mosaicking, we find that the relative source positions (compared to the F200W images) across the different NIRC*am* bands have median offsets of less than 0.07 SW pixels (2 mas) in each direction.

We estimate and subtract any remaining background in the submosaics, following roughly the procedure outlined in Bagley et al. (2023). Specifically, we first generously mask sources and then measure the background in the unmasked regions using the `Photutils Background2D` class. We use the `biweight_location` estimator to obtain the average background in σ -clipped boxes of 10×10 pixels in a grid across the image. The resulting low-resolution background grid is then median-filtered over 5×5 adjacent boxes. We use the `BkgZoomInterpolator` algorithm to interpolate the filtered array and construct a smooth background model.

4. Photometric Catalog

Using our image mosaics (Section 3), we generated a photometric catalog following the procedures described in B. Robertson et al. (2023, in preparation). We provide a brief overview of the detection and photometry methods here, but we refer the reader to B. Robertson et al. (2023, in preparation) for further details.

4.1. Detection

To create a detection image, we produce an image of the NIRC*am* LW signal-to-noise ratio (S/N) as the ratio of signal and noise images. For the signal image, we create an inverse-variance-weighted stack of the SCI flux extensions of F277W, F335M, F356W, F410M, and F444W images. For the noise image, we create an inverse-variance-weighted stack of the ERR uncertainty extensions of the same images but use a median filtering to replace pixels poorly masked by the `jd-st` pipeline. The result is an S/N image that allows for the selection of both faint continuum sources that would be marginally detected in any one filter and strong line emitters present in only a single NIRC*am* LW filter.

The subsequent detection method was inspired by the approach of `NoiseChisel` (Akhlaghi & Ichikawa 2015), which has been effective in analyzing deep images with extended low-surface-brightness features (e.g., Borlaff et al. 2019). Our pipeline implementation written in Python was constructed from `Astropy` (Astropy Collaboration et al. 2022), `Photutils` (Bradley 2023), `scikit-image` (Van der Walt et al. 2014), and `copy` (Okuta et al. 2017) routines. In using `Photutils`, several of the algorithms were adopted from `sExtractor` (Bertin & Arnouts 1996). First, an initial, detection catalog of blended sources is generated by using the `Photutils detect_sources` routine with a minimum threshold of $S/N = 1.5$. A series of binary hole filling, segment expansion, erosion, and morphological opening operations are applied to the resulting segmentation map to reduce spurious noise detections and separate objects blended by narrow, low-surface-brightness bridges. Deblending is performed on the segmentation map using a logarithmically scaled F200W image by iteratively applying image denoising via median filtering, detecting peaks, and then assigning regions of the blended segmentation to individual sources by using a watershed algorithm about the peaks. The largest segments are further deblended using `Photutils deblend_sources` using the parameters `nlevels = 16` and `contrast = 0.1`. We prevent objects from being deblended into sources that lie within the Gaussian-equivalent moments of its light distribution (the ellipse defined by `Photutils semimajor_sigma` and `semiminor_sigma`). Satellites are identified by applying `detect_sources` to the high-pass-filtered outer light distribution of extended sources. Using the segmentation map of these identified objects, we then mask the S/N image and search for compact sources missed or removed by previous operations by performing again `detect_sources` on blank regions with a threshold of $S/N = 3.5$. The last step in defining the segmentation map is to apply a bright star and persistence mask determined from a simple threshold detection applied to an inverse-variance-weighted stack of all JADES images. The mask reblends shredded bright stars, includes diffraction spike segmentations from off-image stars, and covers two regions of strong persistence in the southeastern corner of the mosaic.

The JADES data release includes the segmentation maps that cover the whole of the mosaic footprint with the same pixel scale and WCS header as the images. These segmentation maps are provided in 32-bit integer format, with each segment assigned a unique ID. The source IDs are noncontiguous to preserve consistency between object identifications in previous internal JADES catalogs and have no special meaning.

³² The exact pixel size of the mosaics is $0.0299947'' \text{ pixel}^{-1}$ to match the effective pixel size of the HLF HST mosaics after incorporating a slight correction to improve their registration with respect to Gaia DR2 positions.

4.2. Photometry

The segmentation map produced using the detection method described in Section 4.1 provides the sources we use in constructing our photometric catalog. With the segmentation map defined, the centroids of each object are determined using the `Photutils` implementation of the `sextractor` windowed position algorithm applied to the NIRCcam LW signal image. For each object, the signal image is also used to define the Gaussian-equivalent semimajor and semiminor elliptical sizes, their elliptical orientation on the sky, and the Kron radius. For the Kron radius, we use a Kron parameter of $K = 2.5$ and use `Photutils` to compute the Kron radius from an elliptical region with circularized radius 6 times larger than the Gaussian-equivalent elliptical sizes (i.e., the `Photutils` default) while masking segmentation regions of neighboring sources. For small objects, and especially small objects in regions of enhanced background flux, this method results in artificially inflated Kron apertures that extend well beyond their compact light distribution. We therefore limit Kron apertures to regions twice the area of the object segmentation. As an alternative, we also compute separately apertures with a Kron parameter of $K = 1.2$ and report properties for both apertures.

The JADES photometric catalogs include a variety of flux measurements in different apertures for each source, with forced photometry at the object locations determined by the detection method. We measure circular aperture fluxes within radii of $r = [0''.1, 0''.15, 0''.25, 0''.3, 0''.35, 0''.5]$, which correspond to CIRC1 through CIRC6, respectively. CIRC0 corresponds to the 80% encircled energy radius determined by the point-spread function (PSF) for each filter. We measure flux within the elliptical Kron apertures described above and the sum of the pixel flux values within each object segmentation. This results in 10 separate flux measurements for every source in each filter. The half-light radii for each object are measured relative to the total Kron flux in each band.

Two kinds of flux uncertainties are reported for each of the JADES NIRCcam aperture flux measurements. First, we measure directly the uncertainties from the `jwst` pipeline ERR extension of our mosaics for each aperture. Second, we compute random-aperture-based uncertainties that account for the correlated-noise contribution to the flux error (e.g., Labbé et al. 2005; Quadri et al. 2007; Whitaker et al. 2011; Skelton et al. 2014; Whitaker et al. 2019). For a range of aperture sizes, we measure the spread values in blank areas of each mosaic at 100,000 random locations. Since the image depth can vary dramatically over the field, especially for the HST mosaics, these random apertures are collected into percentiles based on exposure time at each location, and then the power-law scaling between the rms of counts and aperture size is fit for each percentile of apertures and recorded. These scalings are used to determine the sky-noise contribution to the flux uncertainty of each object for each aperture size, with the sky and source Poisson uncertainties added in quadrature to provide the total uncertainty in counts. Combining with the source flux in counts and converting to flux units, the source flux and total uncertainty for every object are then recorded for every aperture reported in the catalog. For the Kron fluxes, the circularized radius of the Kron aperture is used to determine the sky-noise contribution from the measured random-aperture uncertainty scaling relations.

Figure 3 shows an example of the scaling between the rms noise measured in random apertures as a function of aperture

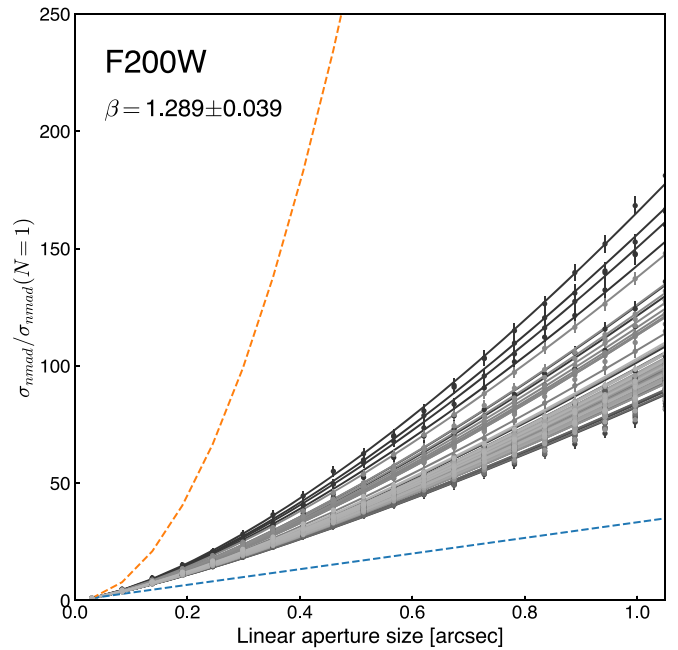


Figure 3. Scaling of blank-sky rms flux within random apertures as a function of aperture diameter. Shown are 100 scalings of the image noise, normalized to the single pixel noise, with linear aperture size for the F200W mosaic where the random apertures are split into percentiles in exposure time. The typical power-law scaling is $\beta = 1.29 \pm 0.04$, compared with the idealized $\beta = 1$ for uncorrelated pixels (blue line) and worst-case $\beta = 2$ for perfectly correlated pixels (orange line).

size for the F200W image. A scaling is measured for each subset of 1000 random apertures in each of the 100 groups split by exposure time percentiles. The index of the power-law scaling is typically $\beta \approx 1.3$ for our images, which is a measure of the degree of pixel covariance in our mosaics. For reference, for perfectly uncorrelated pixels $\beta = 1$, and for perfectly correlated pixels $\beta = 2$. Pixel correlations are difficult to avoid on projected and recombined images, but as judged by these scalings, the overall level of correlated noise present in our images is comparable to or better than other space-based data sets (e.g., Skelton et al. 2014; Whitaker et al. 2019).

For aperture corrections of NIRCcam filters, we use the model PSFs (mPSFs) from Ji et al. (2023) constructed by mosaicking WebbPSF models repeatedly over the field identically to our exposure mosaics and then measuring the average PSF. Circular aperture corrections are determined by computing the encircled flux with radius, while Kron-aperture corrections are computed by summing the mPSF within elliptical apertures for each source. For the HST aperture corrections, we build empirical PSFs (ePSFs) using the `Photutils` `EPSFBuilder` algorithm using a list of stars compiled from the Hubble Legacy Field (HLF; Whitaker et al. 2019) and those determined by the star loci in color–magnitude–size relations.

4.3. Common PSF-matched Images and Photometry

For color selection and spectral energy distribution fitting, measuring source photometry on common PSF-matched images can ameliorate the effect of varying resolution with wavelength on color. For our PSF-matched images, we use the NIRCcam F444W mPSF as our target convolutional kernel. We

generate PSF-matched images for all HST and JWST filters except the target image F444W and the NIRCcam LW F430M, F460M, and F480M images. To generate common PSF images, we use a Wiener filtering method to regularize the convolution by the pixel-level Poisson power σ^2 in blank regions and apply a low-pass filter to reduce high-frequency noise from the HST ePSF and JWST mPSF models. Mathematically, our convolutional kernel is then

$$K(f) = \tilde{P}_i(f) \frac{\tilde{P}_i^*[S(f) - \sigma^2]}{|\tilde{P}_i|^2(S(f) - \sigma^2) + \sigma^2}, \quad (2)$$

where \tilde{P}_i is the Fourier transform of the target (F444W) PSF, \tilde{P}_i is the Fourier transform of the PSF for the image we are convolving, σ^2 is the Poisson per-pixel noise power measured in blank regions, and $S(f)$ is the power spectrum of the total (signal plus noise) image. The \star indicates complex conjugation, and $|\cdot|^2$ represents the absolute square magnitude. This Wiener filtering kernel reduces to a simple deconvolution with P_i and convolution with P_f for a theoretical noise-free image. We apply a Cosine Bell (Phoutils CosineBellWindow) to the kernel in Fourier space before multiplying $K(f)$ by the Fourier transform of the signal image. The parameter α of the Cosine Bell represents the fraction of array values tapered by the window, and when applied to our kernel, larger values of α pass higher frequencies. We set $\alpha = 0.9$ for JWST NIRCcam SW filters, $\alpha = 0.45$ for JWST NIRCcam LW filters, $\alpha = 0.3$ for HST ACS filters, and $\alpha = 0.4$ for HST WFC3 filters. The common PSF-matched images are inspected for numerical artifacts and ePSFs constructed from stars in the images to test the quality of the PSF matching. We find that the ePSF of each common PSF-matched image has an rms width within 10% of the F444W mPSF and the encircled energy curves agree to within $\sim 1\%$ by $r = 0''.3$.

5. Data Properties

With our JADES pipeline image and catalog data products provided as part of this initial release, we present below several characteristics of the data properties and quality. While many detailed tests of the images, photometry, and catalogs are conducted by S. Tacchella et al. (2023, in preparation) and B. Robertson et al. (2023, in preparation), we provide some examples of the data here as a demonstration of its quality and content. We examine the image exposure time distributions (Section 5.1), noise properties (Section 5.2), and source count distribution with magnitude (Section 5.3), and then we present a comparison of JADES to previous deep infrared observations of the field, including a detailed comparison to CANDELS photometry (Section 5.4).

5.1. Exposure Times

The exposure times of the JADES and JEMS imaging vary among the NIRCcam bands. Figure 4 shows the area covered by the JADES F090W, F115W, F150W, F200W, F277W, F335M, F356W, F410M, and F444W and JEMS F182M, F210M, F430M, F460M, and F480M images against the exposure time. The JEMS images cover approximately 10.1 arcmin^2 at depths of $t \geq 13,914 \text{ s}$ in the F430M and F460M bands and $t \geq 27,829 \text{ s}$ in the F182M, F210M, and F480M bands. The JADES images all cover at least 25 arcmin^2 to

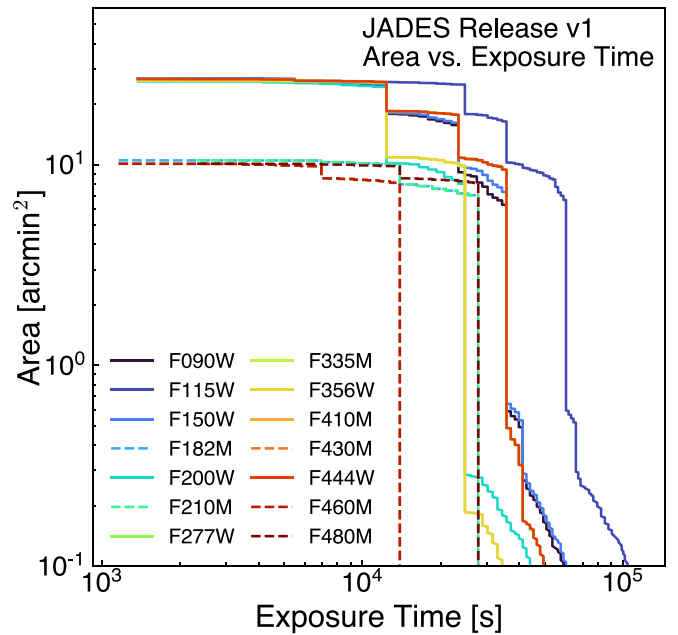


Figure 4. Distribution of exposure times in the JADES NIRCcam F090W, F115W, F150W, F200W, F277W, F335M, F356W, F410M, and F444W and JEMS NIRCcam F182M, F210M, F430M, F460M, and F480M images. Exposure times range from $t \approx 13,900 \text{ s}$ over area $\sim 10 \text{ arcmin}^2$ in F460M to $t \approx 13,700\text{--}60,500 \text{ s}$ over area $\sim 5\text{--}25 \text{ arcmin}^2$ in F115W.

$t \geq 12,300 \text{ s}$. F356W additionally covers at least 10 arcmin^2 to $t \geq 24,736 \text{ s}$. F115W reaches $t \geq 35,731 \text{ s}$ over at least 15 arcmin^2 and $t \geq 60,468 \text{ s}$ over at least 6.7 arcmin^2 . The other JADES bands reach $t \geq 23,300 \text{ s}$ over at least 17 arcmin^2 and $t \geq 35,000 \text{ s}$ over at least 6.3 arcmin^2 .

Figure 5 shows the JADES exposure maps in the F090W, F115W, F150W, F200W, F277W, F335M, F356W, F410M, and F444W filters. The exposure maps reveal the mosaic tiling of the JADES observations in the NIRCcam SW and LW filter. For the SW filters, the masking of persistence and other data quality issues is apparent in each of the F090W, F115W, F150W, and F200W maps. The map morphology also shows the extra exposure time invested in F115W as bright regions.

5.2. Noise Properties

The photometry measured at random locations used in Section 4.2 to define the aperture flux uncertainties in the catalogs reveals the noise properties of the images. While a detailed image quality analysis will be provided by S. Tacchella et al. (2023, in preparation), we provide a few example measurements of image noise properties that demonstrate the high quality of our reduction method.

Figure 6 shows the histogram of flux values for $r = 0''.14$ -radius circular apertures measured in blank regions of the F200W image, before aperture correction. The median background flux measured after 5σ -clipping is $f \approx 0.1 \text{ nJy}$, demonstrating control of the global background subtraction to $\sim 33.8 \text{ AB}$. The rms flux is $\sigma = 0.73 \text{ nJy}$, corresponding to a 5σ depth of 30 AB (before aperture correction). These random apertures can be binned spatially to measure the location-dependent mean and rms noise across each image. Figure 7 shows variations in the mean background measured in small $r = 0''.05$ circular apertures across the F200W image. Regions with lower exposure time have larger spatial variations, especially near the image edges and intermodule regions of

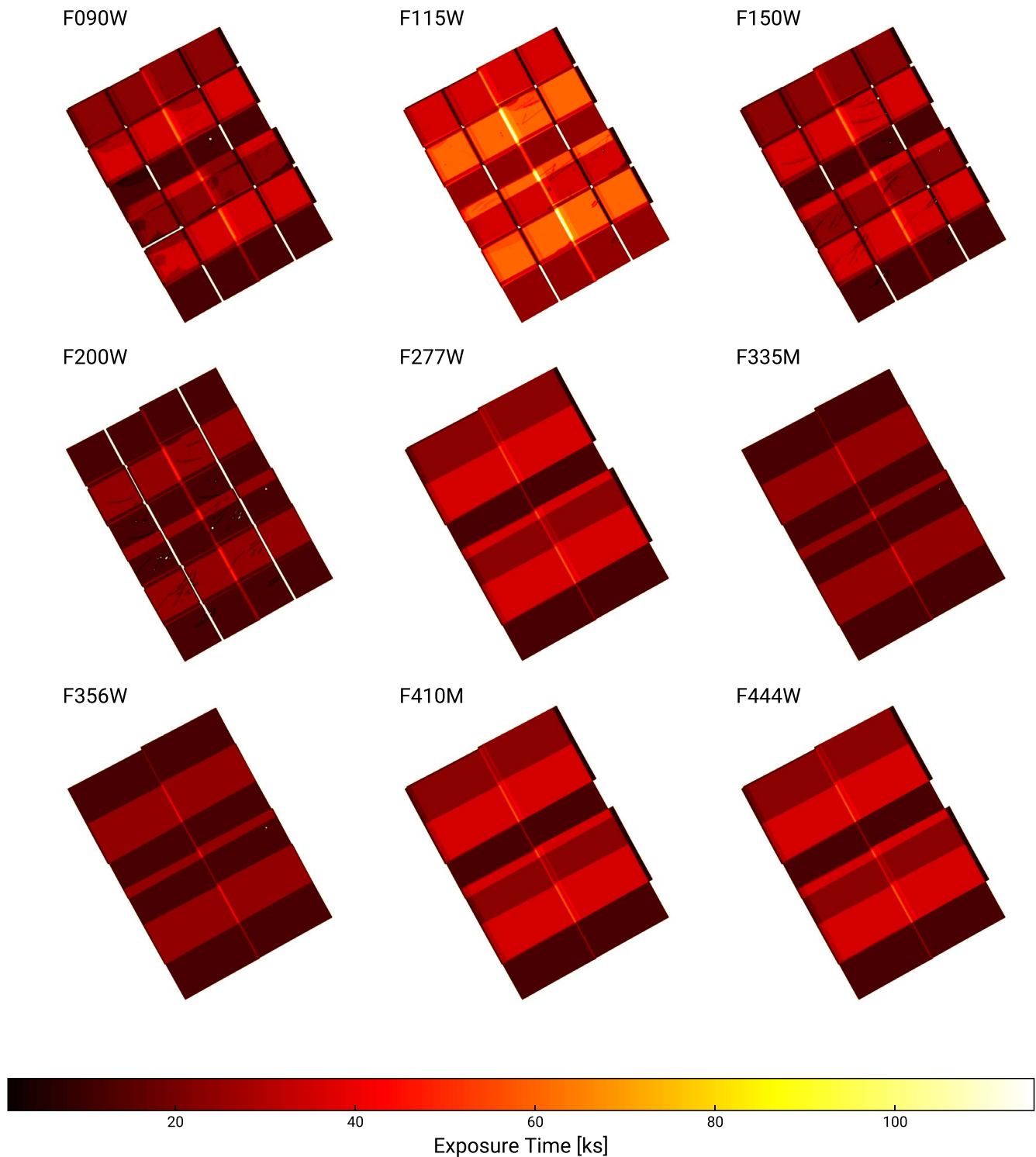


Figure 5. Exposure maps for the JADES NIRCcam mosaics. Shown are the JADES F090W, F115W, F150W, F200W, F277W, F335M, F356W, F410m, and F444W filter exposures. Bright regions indicate areas of increased depth, as reflected by the color-bar scale.

the mosaic, but no strong gradients are present within regions of comparable exposure depth, and the background maintains its zero mean spatially well. The rms of the aperture flux values can also be visualized, as shown in Figure 8, which shows the rms sky noise measured in $r = 0''.11$ circular apertures across the F200W image. The regions of enhanced exposure are apparent as regions with lower rms noise, and the increased noise in intermodule regions with fewer contributing exposures

is also visible. Overall, the noise map shows no gradients in regions of comparable exposure time, and we conclude that the JADES images have quite uniform noise properties. We note that Figures 6, 7, and 8 all intentionally use differing aperture sizes to illustrate the richness of the statistics available for the images. In practice, as part of our data validation, such plots are automatically created and compiled for each aperture size and each filter. These hundreds of plots are visually inspected to

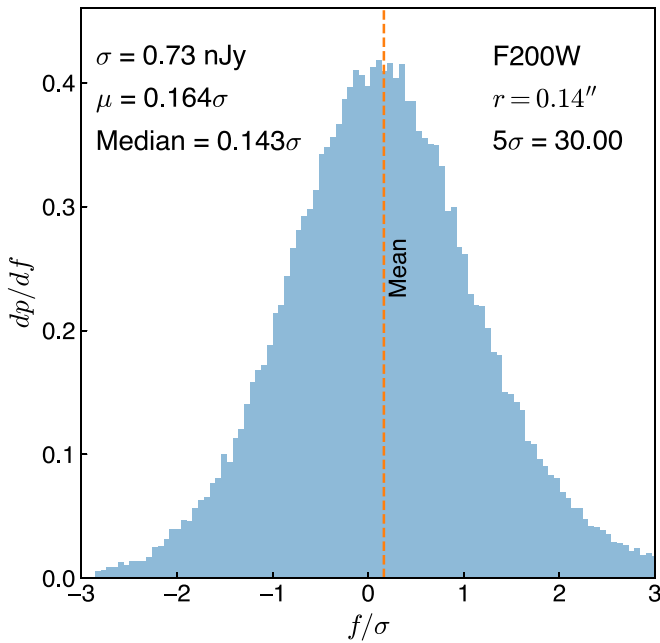


Figure 6. Example blank-sky fluxes measured in randomly distributed $0''.14$ -radius apertures. Shown is the distribution of random-aperture fluxes measured on the F200W mosaic after applying 5σ clipping. The raw statistics of the distribution are listed in the figure. The median background flux is <0.2 nJy. After aperture correction, the rms flux uncertainty in $r = 0''.14$ apertures is ~ 4.3 nJy.

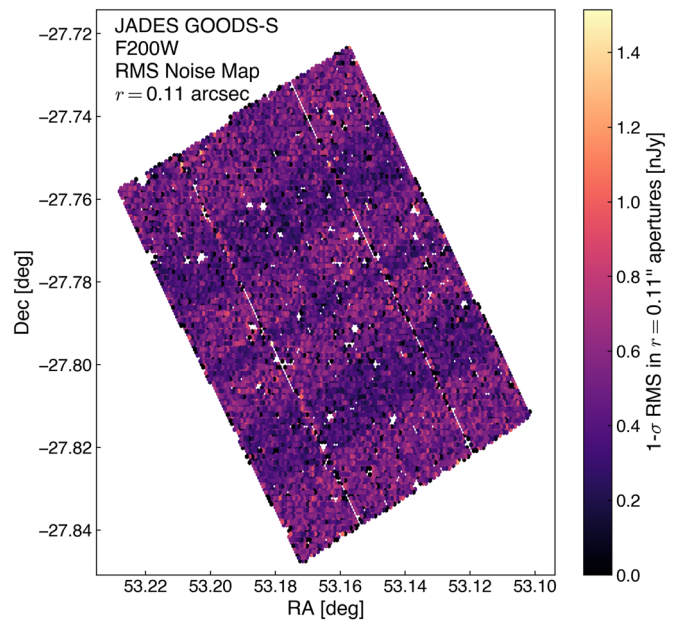


Figure 8. Map of the rms noise across the F200W image, measured in randomly distributed $r = 0''.11$ -radius apertures. The spatial variations in the random-aperture rms flux reflect the exposure time map of F200W.

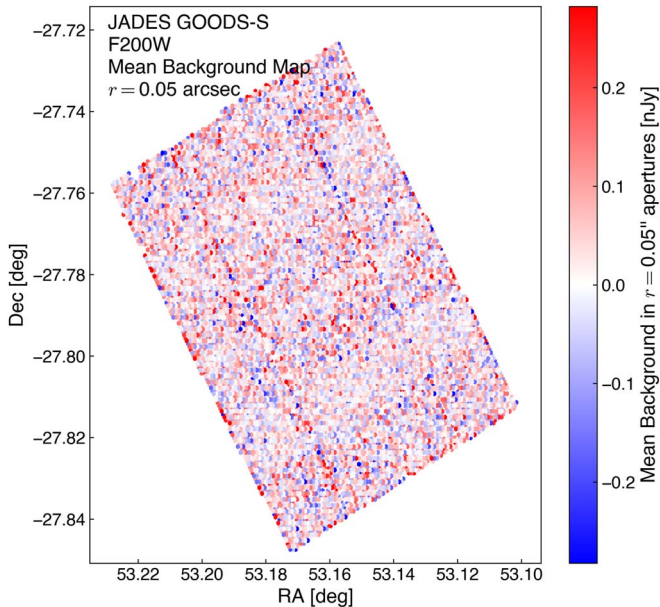


Figure 7. Spatial distribution of the local mean background in the JADES F200W image, measured in $r = 0''.05$ -radius apertures. The mean background over the whole image is $\lesssim 0.1$ nJy, with local variations in the mean background everywhere $\lesssim 0.3$ nJy.

help validate our combined pipeline, identify potential issues in our reductions, and cross-check our data quality between subsequent versions of image reductions and catalogs.

5.3. Source Counts

From the JADES NIRC*am* catalogs, we can construct the distribution of sources as a function of their flux in different

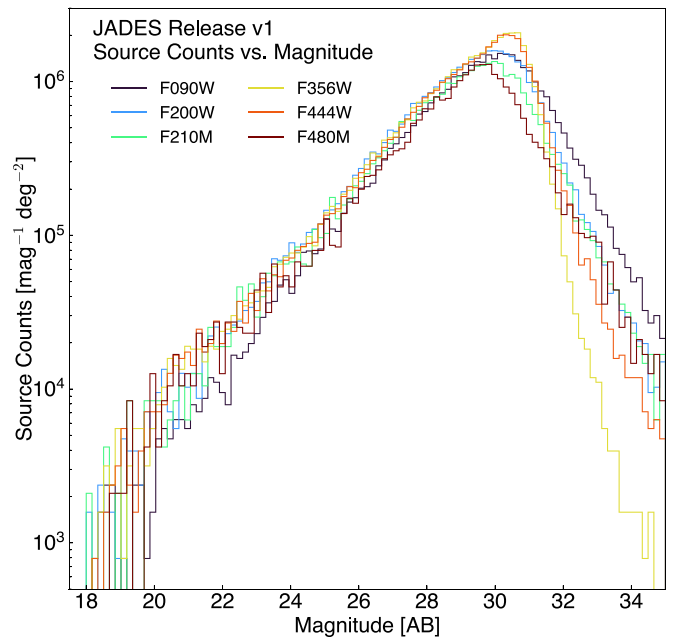


Figure 9. Source counts of objects in the JADES v1 catalog release as a function of object AB magnitude. Shown are the source count distributions for the JADES F090W, F115W, F356W, and F444W bands and the JEMS F210M and F480M bands. The sources plotted are pulled from the JADES multiband detection catalog with forced photometry in each band, such that these histograms contain common sources where their corresponding images overlap spatially. These bands were chosen to cover the range of exposure time vs. area distributions (see Figure 4).

bands. The source count distribution will depend on the image filter owing to the color of sources, which induces a horizontal shift in the distribution, and the image depth that controls the fall-off in source densities toward faint flux levels. Figure 9 shows the number of objects per unit magnitude per square degree as a function of AB magnitude for Kron apertures measured in the F090W, F200W, F210M (JEMS), F356W,

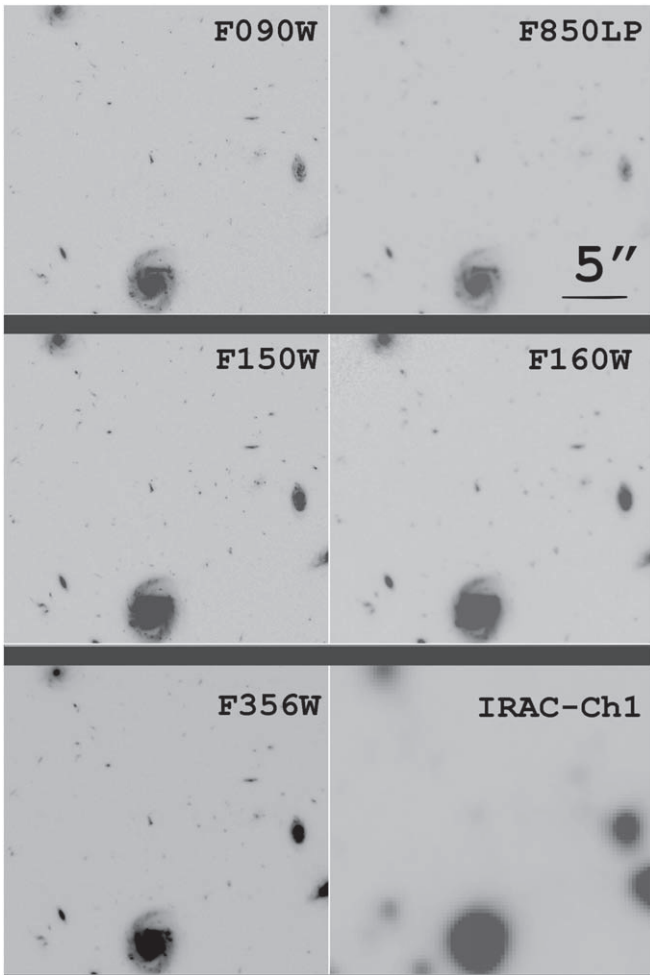


Figure 10. A comparison of JWST imaging to that of HST and Spitzer, using the same small region of the HUDF. Top: the NIRCam F090W image on the left, compared to the HST F850LP image (116 hr; Whitaker et al. 2019) on the right. Middle: the NIRCam F150W image on the left, compared to the HST F160W image (65 hr; Whitaker et al. 2019) on the right. The JWST imaging is notably sharper than that of HST and mildly deeper than even these very long HST exposures. Bottom: the NIRCam F356W image on the left, compared to the Spitzer IRAC Channel 1 $3.6\ \mu\text{m}$ image (Stefanon et al. 2021) on the right. JWST is far deeper and sharper than the deepest Spitzer data.

F444W, and F480M (JEMS) images. The same sources are used in each histogram, with forced photometry applied to the images at source locations as described in Section 4.2. The relative depths of the filter images (see Table 2) are reflected in the location of the histogram peak, and the distribution of exposure times (see Figure 4) affects how rapid the source counts decline once completeness becomes poor.

5.4. Comparison to Other GOODS-S Infrared Data

The data in this release cover portions of the heavily observed GOODS-S field, which provides the HST data that comprise the HLF images we utilize and opportunities for comparisons between published catalogs and our JADES release catalog. A visual impression of the comparison of JADES imaging to that of the deep portion of the HUDF is shown in Figure 10. Here we compare F090W to the HST ACS F850LP imaging and then F150W to the HST WFC3 F160W imaging. Unsurprisingly, the JWST images show a substantially sharper PSF, and JADES is mildly deeper. Of course,

JADES is providing a much wider field, as these deep ACS and WFC3 HST data are only about 11 and 5 arcmin², respectively.

Beyond $1.6\ \mu\text{m}$, JWST is unparalleled, as shown by the comparison of F356W to the imaging at $3.6\ \mu\text{m}$ with Spitzer IRAC (Stefanon et al. 2021). The HUDF is one of the very longest exposures ever with Spitzer, but clearly the sharpness and depth of the JWST imaging are far superior.

To create a quantitative check on our photometry, we focus on the imaging from CANDELS (Grogin et al. 2011; Koekemoer et al. 2011), which imaged a broader area in GOODS-S. We use HST F435W, F606W, F775W, F814W, and F850LP ACS images and F105W, F125W, and F160W WFC3 images that derive from the CANDELS program for measuring blue photometry for the JADES sources. We match sources between the CANDELS catalogs created by Guo et al. (2013) and the JADES catalogs and then compare the measured photometry in each HST filter. Figure 11 shows the histogram of fractional flux difference between the Kron photometry of Guo et al. (2013) and JADES as a function of source AB magnitude in the eight HST filters available in the CANDELS v1 catalog. The relative agreement is excellent, and we compute a median offset in fractional flux difference between CANDELS and JADES of <0.0001 for F606W, degrading to 0.042 in WFC3 F160W. The median offsets are computed for objects brighter than the 5σ flux limit of CANDELS GOODS-S Wide reported by Grogin et al. (2011). We note that we do not use WFC3 in our SED fitting and usually only combine JWST NIRCcam with HST ACS data in our analyses.

As a further check on our photometry, we compare NIRCcam F356W magnitudes in Kron apertures to IRAC Channel 1 magnitudes using PSF fits to data in $3''.6$ apertures presented in Ashby et al. (2015). IRAC Channel 1 has a very similar bandpass to NIRCcam’s F356W filter but has very different spatial resolution, with ~ 400 NIRCcam long-wavelength pixels being equivalent to 1 IRAC pixel. Figure 12 shows this comparison with a relatively small offset between the two data sets. Sources from JADES were matched to IRAC sources requiring object centroids to agree within $0''.2$. The positional requirement is tighter than for the comparison to ACS because confusion in the IRAC data can cause light barycenters to be dragged off the main object. The large scatter is partly due to the S/Ns in the IRAC data and partly because of the resolution difference.

6. Photometric Redshifts

We measure photometric redshifts for the resulting source catalog using the template-fitting code EAZY (Brammer et al. 2008). EAZY combines a set of user-defined galaxy templates to fit the observed photometry for each source across a redshift grid. We adopt the value corresponding to the overall $\chi^2(z)$ minimum as our photometric redshift (z_{phot}) and use the output $P(z)$ surface to estimate uncertainties ($P(z) = \exp[-\chi^2(z)/2]$). For this catalog, we follow the fitting procedure, including the templates and parameters used as described in Hainline et al. (2023).

Because of the large range of redshifts and galaxy sizes in the catalog, we perform fits using the Kron fluxes and uncertainties estimated from the PSF-matched mosaics. We fit to the JADES JWST/NIRCcam F090W, F115W, F150W, F200W, F277W, F335M, F356W, F410M, and F444W photometry. At shorter wavelengths, we combined these data with the HST/ACS F435W, F606W, F775W, F814W, and F850LP fluxes. For a portion of the field where there was overlap, we also added the JEMS JWST/NIRCcam F182M,

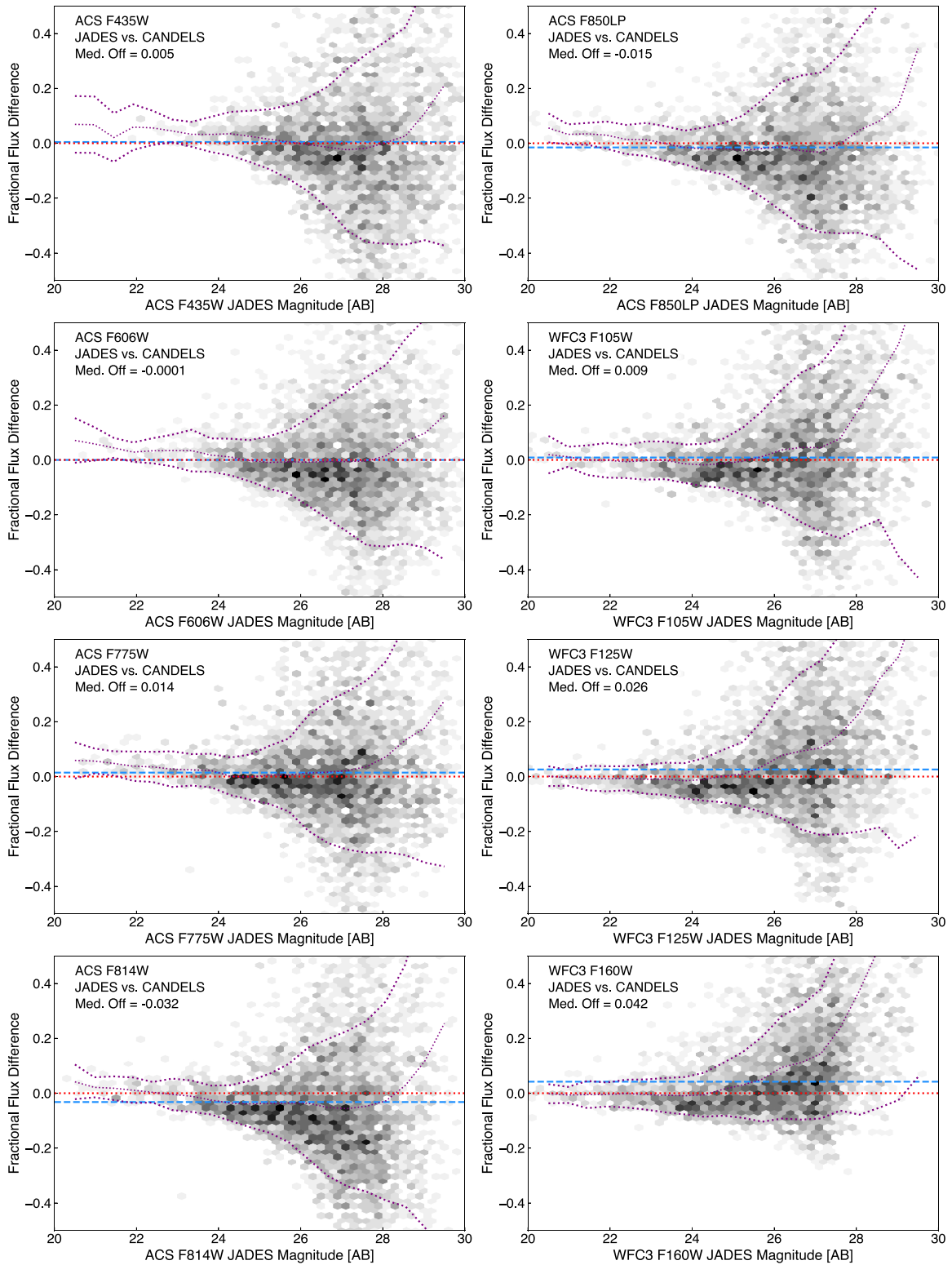


Figure 11. Comparison between JADES photometry on the HLF HST images and the photometry reported by CANDELS (Guo et al. 2013). Shown are histograms of the fractional difference between the JADES Kron-aperture photometry and the total flux reported in v1.0 of the CANDELS multiwavelength catalog, relative to the JADES flux as a function of the JADES AB magnitude. The histograms are measured for objects in the CANDELS catalog with a counterpart in the JADES catalog matched within $0''.5$. Shown are histograms for ACS F435W, F606W, F775W, F814W, and F850LP and WFC3 F105W, F125W, and F160W. We also report the fractional flux median offset between CANDELS and JADES for objects brighter than the 5σ extended object depth reported by Grogin et al. (2011) for each CANDELS band (blue dashed line). We show zero fractional difference with a dotted red line. The dotted purple lines show the running median and $\pm 1\sigma$ spread of each distribution.

F210M, F430M, F460M, and F480M medium-band fluxes. We opted to not use the HST/WFC3 photometry for the fitting because of the poorer spatial resolution and lower S/N.

To demonstrate the accuracy of the estimated photometric redshifts, we collected spectroscopic redshifts from the literature, as well as those measured from an independent

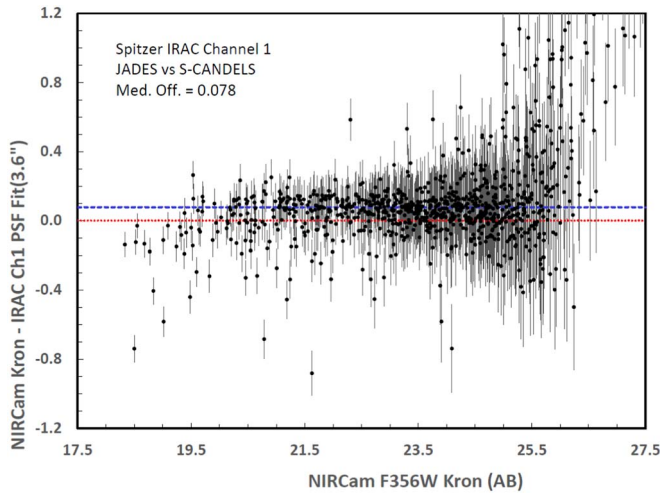


Figure 12. Comparison of JADES F356W photometry with IRAC Channel 1 photometry reported in Ashby et al. (2015). The JADES AB magnitude for Kron radii is plotted against the difference between the JADES AB magnitudes and IRAC data using a PSF fit computed over a $3''$ 6-diameter area. Sources were required to match with $0''.2$ (see text). The blue dashed line indicates the median offset between JADES and IRAC data. Zero difference between the two data sets is indicated by a dotted red line.

reduction of the NIRCam grism data from the FRESCO survey (Oesch et al. 2023) and NIRSpec observations of JADES sources. The FRESCO spectroscopic redshifts will be discussed in F. Sun et al. (2023, in preparation), and the NIRSpec observations are from the JADES “DeepHST” campaign, as presented in Curtis-Lake et al. (2023) and Bunker et al. (2023). The literature spectroscopic redshifts come from multiple sources over the past 20 yr: Daddi et al. (2004), Szokoly et al. (2004), Mignoli et al. (2005), van der Wel et al. (2005), Ravikumar et al. (2007), Vanzella et al. (2008, 2009), Wuyts et al. (2008), Balestra et al. (2010), Silverman et al. (2010), Xue et al. (2011), Cooper et al. (2012), Kurk et al. (2013), Le Fèvre et al. (2013), Trump et al. (2013), Kriek et al. (2015), Le Fèvre et al. (2015), Morris et al. (2015), Momcheva et al. (2016), McLure et al. (2018), Pentericci et al. (2018a), Pentericci et al. (2018b), Wisnioski et al. (2019), and Garilli et al. (2021). We also used spectroscopic redshifts from the MUSE_HUDF (Inami et al. 2017), MUSE_WIDE (Urrutia et al. 2019), and MUSE_DR2 (Bacon et al. 2023) surveys, and we separate those out from the rest of the literature sources. For each we only chose to compare against those spectroscopic redshifts with the most confident quality flags.

Our final spectroscopic redshift catalog consists of 263 sources from the assembled literature catalogs, 869 from MUSE, 147 from our measurements from FRESCO data, and 150 from NIRSpec. In total there are 1429 sources (57 arcmin^{-2}) with spectroscopic redshifts. In Figure 13, we plot our estimated photometric redshifts against the assembled spectroscopic redshifts. We color the points by the source of the spectroscopic redshift, and in the legend we provide the number of sources, the number of catastrophic outliers, and the outlier fraction, defined as the number of objects with $|z_{\text{spec}} - z_{\text{phot}}| / (1 + z_{\text{spec}}) > 0.15$. At the top we provide the statistics for the overall sample.

The comparison of the photometric redshifts to the spectroscopic redshifts is highly encouraging: we only find 68 catastrophic outliers, for an overall outlier fraction of 5%. In many of the catastrophic outliers, the EAZY χ^2 surface has two

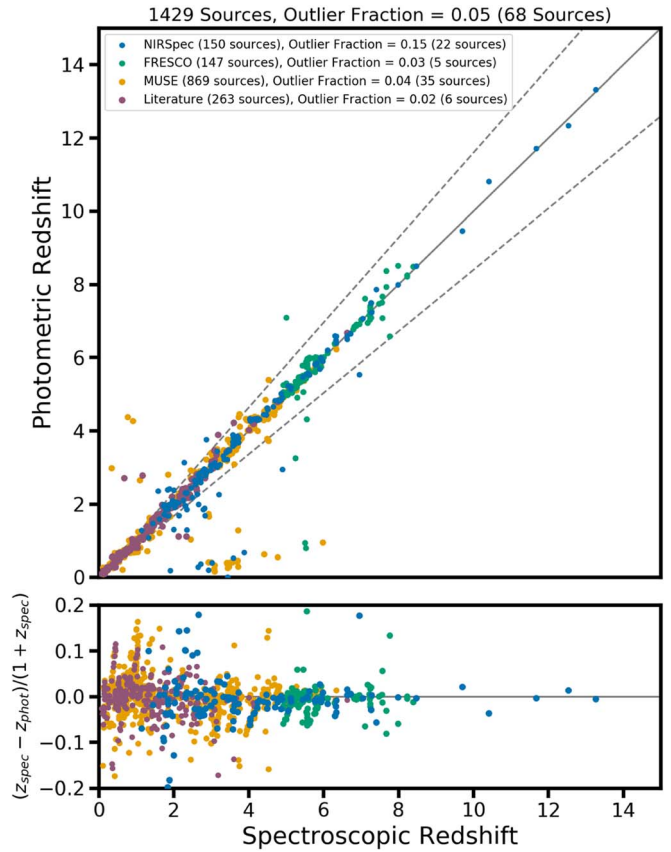


Figure 13. Photometric redshifts plotted against spectroscopic redshifts. The photometric redshifts were calculated using the PSF-convolved mosaics and Kron elliptical aperture fluxes. We color the points by whether they are in the broad literature of GOODS-S spectroscopic redshifts (dark pink), or whether they are derived from MUSE observations (gold), FRESCO observations (green), or NIRSpec observations (blue). We find an overall outlier fraction of 5%, $\langle z_{\text{spec}} - z_{\text{phot}} \rangle = 0.05$, $\sigma_{\text{NMAD}} = 0.024$. The cloud of points at $z_{\text{spec}} = 3\text{--}4$ and at $z_{\text{phot}} = 0\text{--}1$ are those sources where the Lyman break has been mistaken as the Balmer break in the fit.

minima and the photometry supports an incorrect photometric redshift solution. In addition, we measure the average offset between the photometric redshifts and the spectroscopic redshifts, $\langle z_{\text{spec}} - z_{\text{phot}} \rangle = 0.05$, and the scatter around the relation, $\sigma_{\text{NMAD}} = 0.024$, defined as

$$\sigma_{\text{NMAD}} = 1.48 \times \text{median} \left(\left| \frac{\delta z - \text{median}(\delta z)}{1 + z_{\text{spec}}} \right| \right), \quad (3)$$

where $\delta z = z_{\text{spec}} - z_{\text{phot}}$. While the sources with high-quality spectroscopic redshifts are brighter than the bulk of the population in our sample, we do not see any evidence of systematic trends in the quality of our photometric redshifts. We do observe that the quality of the photometric redshifts is worse at $z_{\text{spec}} < 6$, but this is to be expected, as the Lyman break is covered by the HST/ACS filters at these redshifts at lower sensitivities and smaller exposure times. In addition, for galaxies at $z_{\text{spec}} > 5$, Spitzer/IRAC colors revealed that galaxies have very high equivalent width emission lines (e.g., Smit et al. 2014, 2015; Roberts-Borsani et al. 2016; Stark 2016), which improve photometric redshifts significantly when properly included in templates. In Figure 14 we plot the observed F277W Kron magnitude against the spectroscopic

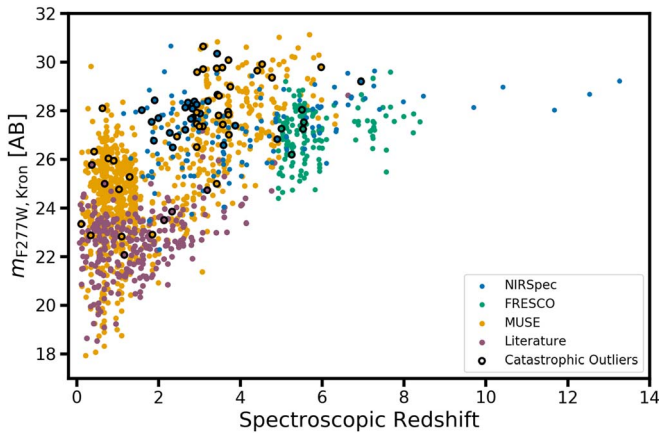


Figure 14. F277W Kron magnitude plotted against spectroscopic redshifts. We plot the objects in each category of spectroscopic redshifts with the same colors as in Figure 13. We also plot catastrophic outliers in the photometric redshift vs. spectroscopic redshift plot with black outlines on the points. We can see that the observed F277W magnitudes for the spectroscopic redshift comparison sample extend across a wide range and that many of the $z > 3$ catastrophic outliers are faint sources.

redshift and highlight the catastrophic outliers seen in Figure 13. We can see that our sources with spectroscopic redshifts span a range of magnitudes $m_{F277W, \text{Kron}} = 18\text{--}30$ and that primarily our outliers at $z > 3$ are fainter galaxies.

7. Conclusions and Data Access

We have described the first NIRCам data release from JADES, which provides very deep nine-band infrared imaging of 26 arcmin² fully covering the HUDF. This brings the exquisite sensitivity and angular resolution of JWST to this premier deep field. Combined with JEMS and previous HST data, there are 24 bands of space-quality optical and near-infrared imaging, revealing galaxies with great detail in their colors and morphologies.

The imaging and catalogs from this release are available at <https://archive.stsci.edu/hlsp/jades>. This site also includes details of the catalog contents. Further, at <http://jades.idies.jhu.edu/> we provide a link to our FITSmap (Hausen & Robertson 2022) visualization of the data, where one can pan and zoom in on multiple filters and use overlays to present the associated catalog data. We have found these to be extremely useful in browsing the data and in probing issues in the data reduction.

This is the first of several upcoming releases from JADES. As described in Eisenstein et al. (2023), future work will expand the GOODS-S footprint and explore GOODS-N. In cycle 2, the footprint of this UDF region will be observed again, roughly doubling the depth and providing for a 1 yr return to study the variability of the deep infrared sky, and we will conduct extensive spectroscopy in the field.

We hope that this release from JADES, as well as the companion NIRCам release (Bunker et al. 2023), will provide an important community resource for the study of the HUDF, including for the upcoming Cycle 3 proposal cycle. The JADES data are fulfilling the dream of pushing back the redshift frontier to the first galaxies as envisaged by the early proponents of the JWST mission.

Acknowledgments

The JADES Collaboration thanks the Instrument Development Teams and the instrument teams at the European Space Agency and the Space Telescope Science Institute for the support that made this program possible. We also thank our program coordinators at STScI for their help in planning complicated parallel observations.

M.R., A.D., C.D., E.E., D.J.E., B.D.J., B.R., G.R., F.S., D. S., Z.C., L.W., and C.N.A.W. acknowledge support from the NIRCам Science Team contract to the University of Arizona, NAS5-02015. D.J.E. is further supported as a Simons Investigator. S.Ar. acknowledges support from grant PID2021-127718NB-I00 funded by the Spanish Ministry of Science and Innovation/State Agency of Research (MICIN/AEI/ 10.13039/501100011033). A.J.B., A.J.C., J.C., A.S., and I.E.B.W. acknowledge funding from the “FirstGalaxies” Advanced Grant from the European Research Council (ERC) under the European Union’s Horizon 2020 research and innovation program (grant agreement No. 789056). A.J.C. acknowledges funding from the “FirstGalaxies” Advanced Grant from the European Research Council (ERC) under the European Union’s Horizon 2020 research and innovation program (grant agreement No. 789056).

Funding for this research was provided by the Johns Hopkins University, Institute for Data Intensive Engineering and Science (IDIES). R.M., W.B., F.D.E., T.J.L., L.S., and J. W. acknowledge support by the Science and Technology Facilities Council (STFC) and by the ERC through Advanced grant 695671 “QUENCH.” R.M. also acknowledges funding from a research professorship from the Royal Society. J.W. further acknowledges support from the Fondation MERAC. The research of C.C.W. is supported by NOIRLab, which is managed by the Association of Universities for Research in Astronomy (AURA) under a cooperative agreement with the National Science Foundation. A.L.D. thanks the University of Cambridge Harding Distinguished Postgraduate Scholars Programme and Technology Facilities Council (STFC) Center for Doctoral Training (CDT) in Data intensive science at the University of Cambridge (STFC grant No. 2742605) for a PhD studentship. R.S. acknowledges support from an STFC Ernest Rutherford Fellowship (ST/S004831/1). C.Wo. is supported by the National Science Foundation through the Graduate Research Fellowship Program funded by grant award No. DGE-1746060.

D.P. acknowledges support by the Huo Family Foundation through a P.C. Ho PhD Studentship. H.Ü. gratefully acknowledges support by the Isaac Newton Trust and by the Kavli Foundation through a Newton–Kavli Junior Fellowship. L.W. acknowledges support from the National Science Foundation Graduate Research Fellowship under grant No. DGE-2137419. R.E.H. acknowledges support from the National Science Foundation Graduate Research Fellowship Program under grant No. DGE-1746060. S.C. acknowledges support by European Union’s HE ERC Starting grant No. 101040227—WINGS. The research of K.B. is supported in part by the Australian Research Council Centre of Excellence for All Sky Astrophysics in 3 Dimensions (ASTRO 3D), through project No. CE170100013.

Processing for the JADES NIRCам data release was performed on the *lux* cluster at the University of California, Santa Cruz, funded by NSF MRI grant AST 1828315. This work was performed using resources provided by the

Cambridge Service for Data Driven Discovery (CSD3) operated by the University of Cambridge Research Computing Service (www.csd3.cam.ac.uk), provided by Dell EMC and Intel using Tier-2 funding from the Engineering and Physical Sciences Research Council (capital grant EP/T022159/1), and DiRAC funding from the Science and Technology Facilities Council (www.dirac.ac.uk). Support for program JWST-GO-1963 was provided in part by NASA through a grant from the Space Telescope Science Institute, which is operated by the Associations of Universities for Research in Astronomy, Incorporated, under NASA contract NAS 5-26555.

ORCID iDs

Marcia J. Rieke <https://orcid.org/0000-0002-7893-6170>
 Brant Robertson <https://orcid.org/0000-0002-4271-0364>
 Sandro Tacchella <https://orcid.org/0000-0002-8224-4505>
 Kevin Hainline <https://orcid.org/0000-0003-4565-8239>
 Benjamin D. Johnson <https://orcid.org/0000-0002-9280-7594>
 Ryan Hausen <https://orcid.org/0000-0002-8543-761X>
 Zhiyuan Ji <https://orcid.org/0000-0001-7673-2257>
 Christopher N. A. Willmer <https://orcid.org/0000-0001-9262-9997>
 Daniel J. Eisenstein <https://orcid.org/0000-0002-2929-3121>
 Dávid Puskás <https://orcid.org/0000-0001-8630-2031>
 Stacey Alberts <https://orcid.org/0000-0002-8909-8782>
 Santiago Arribas <https://orcid.org/0000-0001-7997-1640>
 William M. Baker <https://orcid.org/0000-0003-0215-1104>
 Stefi Baum <https://orcid.org/0000-0002-4735-8224>
 Rachana Bhatawdekar <https://orcid.org/0000-0003-0883-2226>
 Nina Bonaventura <https://orcid.org/0000-0001-8470-7094>
 Kristan Boyett <https://orcid.org/0000-0003-4109-304X>
 Andrew J. Bunker <https://orcid.org/0000-0002-8651-9879>
 Alex J. Cameron <https://orcid.org/0000-0002-0450-7306>
 Stefano Carniani <https://orcid.org/0000-0002-6719-380X>
 Stephane Charlot <https://orcid.org/0000-0003-3458-2275>
 Jacopo Chevallard <https://orcid.org/0000-0002-7636-0534>
 Zuyi Chen <https://orcid.org/0000-0002-2178-5471>
 Mirko Curti <https://orcid.org/0000-0002-2678-2560>
 Emma Curtis-Lake <https://orcid.org/0000-0002-9551-0534>
 A. Lola Danhaive <https://orcid.org/0000-0002-9708-9958>
 Christa DeCoursey <https://orcid.org/0000-0002-4781-9078>
 Alan Dressler <https://orcid.org/0000-0002-6317-0037>
 Eiichi Egami <https://orcid.org/0000-0003-1344-9475>
 Ryan Endsley <https://orcid.org/0000-0003-4564-2771>
 Jakob M. Helton <https://orcid.org/0000-0003-4337-6211>
 Raphael E. Hviding <https://orcid.org/0000-0002-4684-9005>
 Nimisha Kumari <https://orcid.org/0000-0002-5320-2568>
 Tobias J. Looser <https://orcid.org/0000-0002-3642-2446>
 Jianwei Lyu <https://orcid.org/0000-0002-6221-1829>
 Roberto Maiolino <https://orcid.org/0000-0002-4985-3819>
 Michael V. Maseda <https://orcid.org/0000-0003-0695-4414>
 Erica J. Nelson <https://orcid.org/0000-0002-7524-374X>
 George Rieke <https://orcid.org/0000-0003-2303-6519>
 Hans-Walter Rix <https://orcid.org/0000-0003-4996-9069>
 Lester Sandles <https://orcid.org/0000-0001-9276-7062>
 Aayush Saxena <https://orcid.org/0000-0001-5333-9970>
 Katherine Sharpe <https://orcid.org/0000-0001-8225-8969>
 Irene Shivaie <https://orcid.org/0000-0003-4702-7561>
 Maya Skarbinski <https://orcid.org/0009-0004-0844-0657>
 Renske Smit <https://orcid.org/0000-0001-8034-7802>

Daniel P. Stark <https://orcid.org/0000-0001-6106-5172>
 Meredith Stone <https://orcid.org/0000-0002-9720-3255>
 Katherine A. Suess <https://orcid.org/0000-0002-1714-1905>
 Fengwu Sun <https://orcid.org/0000-0002-4622-6617>
 Michael Topping <https://orcid.org/0000-0001-8426-1141>
 Hannah Übler <https://orcid.org/0000-0003-4891-0794>
 Natalia C. Villanueva <https://orcid.org/0000-0001-6917-4656>
 Imaan E. B. Wallace <https://orcid.org/0000-0002-0695-8485>
 Christina C. Williams <https://orcid.org/0000-0003-2919-7495>
 Chris Willott <https://orcid.org/0000-0002-4201-7367>
 Lily Whitler <https://orcid.org/0000-0003-1432-7744>
 Joris Witstok <https://orcid.org/0000-0002-7595-121X>
 Charity Woodrum <https://orcid.org/0000-0001-5962-7260>

References

- Akhlaghi, M., & Ichikawa, T. 2015, *ApJS*, 220, 1
 Aravena, M., Decarli, R., Walter, F., et al. 2016, *ApJ*, 833, 68
 Ashby, M. L. N., Willner, S. P., Fazio, G. G., et al. 2015, *ApJS*, 218, 33
 Astropy Collaboration, Price-Whelan, A. M., Lim, P. L., et al. 2022, *ApJ*, 935, 167
 Bacon, R., Brinchmann, J., Conseil, S., et al. 2023, *A&A*, 670, A4
 Bacon, R., Conseil, S., Mary, D., et al. 2017, *A&A*, 608, A1
 Bacon, R., Mary, D., Garel, T., et al. 2021, *A&A*, 647, A107
 Bagley, M. B., Finkelstein, S. L., Koekemoer, A. M., et al. 2023, *ApJL*, 946, L12
 Balestra, I., Mainieri, V., Popesso, P., et al. 2010, *A&A*, 512, A12
 Barbary, K. 2016, *JOSS*, 1, 58
 Beckwith, S. V. W., Stiavelli, M., Koekemoer, A. M., et al. 2006, *AJ*, 132, 1729
 Bertin, E., & Arnouts, S. 1996, *A&AS*, 117, 393
 Borlaff, A., Trujillo, I., Román, J., et al. 2019, *A&A*, 621, A133
 Bouwens, R. J., Illingworth, G. D., Oesch, P. A., et al. 2010, *ApJL*, 709, L133
 Bradley, L. 2023, *astropy/photutils: v1.8.0*, Zenodo, doi:10.5281/zenodo.7946442
 Brammer, G. B., van Dokkum, P. G., Coppi, P., et al. 2008, *ApJ*, 686, 1503
 Bunker, A., Cameron, A. J., Curtis-Lake, E., et al. 2023, *A&A*, submitted
 Conselice, C. J., Bluck, A. F. L., Buitrago, F., et al. 2011, *MNRAS*, 413, 80
 Cooper, M. C., Yan, R., Dickinson, M., et al. 2012, *MNRAS*, 425, 2116
 Curtis-Lake, E., Carniani, S., Cameron, A., et al. 2023, *NatAs*, 7, 622
 Daddi, E., Cimatti, A., Renzini, A., et al. 2004, *ApJ*, 617, 746
 Dunlop, J. S., McLure, R. J., Biggs, A. D., et al. 2017, *MNRAS*, 466, 861
 Eisenstein, D., Willott, C., Alberts, S., et al. 2023, *ApJS*, submitted
 Ellis, R. S., McLure, R. J., Dunlop, J. S., et al. 2013, *ApJL*, 763, L7
 Ferguson, H. C., Dickinson, M., & Williams, R. 2000, *ARA&A*, 38, 667
 Gaia Collaboration, Brown, A. G. A., Vallenari, A., et al. 2018, *A&A*, 616, A1
 Gardner, J. P., Mather, J. C., Abbott, R., et al. 2023, *PASP*, 135, 068001
 Garilli, B., McLure, R., Pentericci, L., et al. 2021, *A&A*, 647, A150
 Giacconi, R., Zirm, A., Wang, J., et al. 2002, *ApJS*, 139, 369
 Giavalisco, M., Ferguson, H. C., Koekemoer, A. M., et al. 2004, *ApJL*, 600, L93
 Grogin, N. A., Kocevski, D. D., Faber, S. M., et al. 2011, *ApJS*, 197, 35
 Guo, Y., Ferguson, H. C., Giavalisco, M., et al. 2013, *ApJS*, 207, 24
 Hainline, K. N., Robertson, B., Tacchella, S., et al. 2023, *ApJS*, submitted
 Hatsukade, B., Kohno, K., Yamaguchi, Y., et al. 2018, *PASJ*, 70, 105
 Hausen, R., & Robertson, B. E. 2022, *A&C*, 39, 100586
 Illingworth, G. D., Magee, D., Oesch, P. A., et al. 2013, *ApJS*, 209, 6
 Inami, H., Bacon, R., Brinchmann, J., et al. 2017, *A&A*, 608, A2
 Ji, Z., Williams, C. C., Tacchella, S., et al. 2023, arXiv:2305.18518
 Koekemoer, A. M., Faber, S. M., Ferguson, H. C., et al. 2011, *ApJS*, 197, 36
 Kriek, M., Shapley, A. E., Reddy, N. A., et al. 2015, *ApJS*, 218, 15
 Kurk, J., Cimatti, A., Daddi, E., et al. 2013, *A&A*, 549, A63
 Labbé, I., Huang, J., Franx, M., et al. 2005, *ApJL*, 624, L81
 Le Fèvre, O., Cassata, P., Cucciati, O., et al. 2013, *A&A*, 559, A14
 Le Fèvre, O., Tasca, L. A. M., Cassata, P., et al. 2015, *A&A*, 576, A79
 McLure, R. J., Pentericci, L., Cimatti, A., et al. 2018, *MNRAS*, 479, 25
 Mignoli, M., Cimatti, A., Zamorani, G., et al. 2005, *A&A*, 437, 883
 Momcheva, I. G., Brammer, G. B., van Dokkum, P. G., et al. 2016, *ApJS*, 225, 27

- Morris, A. M., Kocevski, D. D., Trump, J. R., et al. 2015, *AJ*, 149, 178
- Oesch, P. A., Bouwens, R. J., Illingworth, G. D., et al. 2010, *ApJL*, 709, L16
- Oesch, P. A., Brammer, G., Naidu, R. P., et al. 2023, *MNRAS*, 525, 2864
- Okuta, R., Unno, Y., Nishino, D., Hido, S., Loomis, C., et al. 2017, Proc. of Workshop on Machine Learning Systems (LearningSys) in The 31st Annual Conf. on Neural Information Processing Systems (NIPS), http://learningsys.org/nips17/assets/papers/paper_16.pdf
- Pentericci, L., McLure, R. J., Garilli, B., et al. 2018a, *A&A*, 616, A174
- Pentericci, L., Vanzella, E., Castellano, M., et al. 2018b, *A&A*, 619, A147
- Quadri, R., Marchesini, D., van Dokkum, P., et al. 2007, *AJ*, 134, 1103
- Ravikumar, C. D., Puech, M., Flores, H., et al. 2007, *A&A*, 465, 1099
- Rigby, J., Perrin, M., McElwain, M., et al. 2023, *PASP*, 135, 048001
- Roberts-Borsani, G. W., Bouwens, R. J., Oesch, P. A., et al. 2016, *ApJ*, 823, 143
- Robertson, B. E., Tacchella, S., Johnson, B. D., et al. 2023, *NatAs*, 7, 611
- Rujopakarn, W., Dunlop, J. S., Rieke, G. H., et al. 2016, *ApJ*, 833, 12
- Schlawin, E., Leisenring, J., Misselt, K., et al. 2020, *AJ*, 160, 231
- Silverman, J. D., Mainieri, V., Salvato, M., et al. 2010, *ApJS*, 191, 124
- Skelton, R. E., Whitaker, K. E., Momcheva, I. G., et al. 2014, *ApJS*, 214, 24
- Smit, R., Bouwens, R. J., Franx, M., et al. 2015, *ApJ*, 801, 122
- Smit, R., Bouwens, R. J., Labbé, I., et al. 2014, *ApJ*, 784, 58
- Stark, D. P. 2016, *ARA&A*, 54, 761
- Stefanon, M., Labbé, I., Oesch, P. A., et al. 2021, *ApJS*, 257, 68
- Szokoly, G. P., Bergeron, J., Hasinger, G., et al. 2004, *ApJS*, 155, 271
- Thompson, R. I., Storrie-Lombardi, L. J., Weymann, R. J., et al. 1999, *AJ*, 117, 17
- Trump, J. R., Hsu, A. D., Fang, J. J., et al. 2013, *ApJ*, 763, 133
- Urrutia, T., Wisotzki, L., Kerutt, J., et al. 2019, *A&A*, 624, A141
- Van der Walt, S., Schönberger, J. L., Nunez-Iglesias, J., et al. 2014, *PeerJ*, 2, e453
- van der Wel, A., Franx, M., van Dokkum, P. G., et al. 2005, *ApJ*, 631, 145
- Vanzella, E., Cristiani, S., Dickinson, M., et al. 2008, *A&A*, 478, 83
- Vanzella, E., Giavalisco, M., Dickinson, M., et al. 2009, *ApJ*, 695, 1163
- Walter, F., Decarli, R., Aravena, M., et al. 2016, *ApJ*, 833, 67
- Whitaker, K. E., Ashas, M., Illingworth, G., et al. 2019, *ApJS*, 244, 16
- Whitaker, K. E., Labbé, I., van Dokkum, P. G., et al. 2011, *ApJ*, 735, 86
- Williams, C. C., Tacchella, S., Maseda, M. V., et al. 2023, *ApJS*, 268, 64
- Williams, R. E., Blacker, B., Dickinson, M., et al. 1996, *AJ*, 112, 1335
- Wisnioski, E., Förster Schreiber, N. M., Fossati, M., et al. 2019, *ApJ*, 886, 124
- Wuyts, S., Labbé, I., Förster Schreiber, N. M., et al. 2008, *ApJ*, 682, 985
- Xue, Y. Q., Luo, B., Brandt, W. N., et al. 2011, *ApJS*, 195, 10
- Xue, Y. Q., Luo, B., Brandt, W. N., et al. 2016, *ApJS*, 224, 15